Sensitivity of Shading Calculations to Horizon Uncertainty

Joseph Ranalli, Robert Vitagliano, Mauro Notaro and David Starling
Penn State Hazleton

Abstract

Planning for solar power installations requires assessment of potential shading by nearby obstacles on the horizon. A degree of uncertainty exists in measurements of the horizon from the point-of-view of the proposed solar collector. This uncertainty takes the form of errors in the measurement of the azimuth and altitude of obstacles that may cause shading. We modelled irradiance reductions due to shading simulated horizon position measurement uncertainty. Results indicate that the sensitivity of solar simulations to horizon measurements is relatively low (around 2% per degree error for the most sensitive case observed). Beam and diffuse irradiance showed similar sensitivity to horizon measurement errors, and experienced similar trends in sensitivity relative to azimuth and altitude errors. For all cases, sensitivity to altitude errors was observed to be greater than sensitivity to azimuth errors. Conservative estimates of uncertainty in predicted irradiance based upon an existing measurement technique were around 3%.

Keywords: shading; horizon measurement; irradiance uncertainty

Symbols
f – shading factor (beam or diffuse)
G – irradiance (see subscripts below)
θ – angle of incidence between sun and collector surface normal
α_s – solar altitude angle
γ_s – solar azimuth angle
γ_c – collector azimuth angle
α_h –altitude angle of a point in the horizon list
γ_h –azimuth angle of a point in the horizon list
β – collector tilt angle
σ – standard deviation (uncertainty)
φ_c – Obstacle central azimuth
φ_h – Obstacle angular height
φ_w – Obstacle azimuthal width

Subscripts for irradiance, G
x_b – beam component
x_d – diffuse component
x_g – ground reflected component
x_t – irradiance on tilted surface
x_{sh} – shaded irradiance (otherwise assumed to be unshaded)

1. Introduction

In December 2015, the United Nations Framework Convention on Climate Change recognized the "urgent and potentially irreversible threat to human societies and the planet" posed by climate change (United Nations, 2015). Exploitation of renewable energy resources is an important response to the worldwide call for action aimed at reversing the climate change trend. Solar photovoltaics (PV) represent one technology market with room for growth relative to this sustainable energy need. The International Energy Agency reports that in 2014, there were a cumulative 177 GW of solar capacity installed worldwide (accounting for roughly 1% of global demand), with around 40 GW having been installed in that year (International Energy Agency, 2015). The IEA also reports that three countries (Italy, Greece, Germany) produce more than 7% of their electricity demand via PV.

When it comes to economics, renewable energy technologies are typically characterized by high initial equipment costs, with low (in some cases, negligible) operating costs as compared to traditional, fuel-based energy production. As a result, life-cycle cost analysis methods must usually be used to demonstrate the practical economic case for these installations. To support the proliferation of solar development, design level tools have been developed to assist in prediction of the lifetime energy production, costs and savings associated with a proposed PV installation. Due to the long-term nature of the payback, these predictions usually consist of twenty year, or longer, simulations of the proposed system. The ability to accurately and reliably predict the inputs to these simulations, specifically the solar resource during the timespan, is viewed as one of the primary risks from the perspective of those who provide financing for solar installations (Vignola et al., 2012). Vignola et al. propose a methodology by which "bankable" resource data can be obtained, resulting in predictions with higher confidence levels that reduce the risk of uncertainty in the resource.

Solar resource datasets are based upon satellite or ground based observations of the irradiance over time. In general, these datasets are thus unable to account for obstructions that may impede the direct sunlight from reaching the collector on a site-by-site basis. The topography of the proposed site, which serves as the origin for shading of the collector, therefore presents an additional factor in PV output predictions. This shading is of special importance for PV technologies, because the electrical characteristics of PV result in a nonlinear response to shading; a small fraction of a PV panel being shaded may result in a dramatic reduction in the power output. Hanson et al. (Hanson et al., 2014) report that on a sample of 542 arrays, an average of 8.3% loss due to shading was observed. Approaches exist to model shading of PV arrays. One approach involves the measurement of obstructions from the point of view of the collector, which we term the local horizon, for each proposed solar installation site (Goss et al., 2014). This process is commonly known as a site evaluation or site survey (Galli and Hoberg, 2009). Several technical and practical limitations may prohibit highly detailed site survey measurements from being made, introducing potential uncertainties into the horizon observation. MacAlpine and Deline (MacAlpine and Deline, 2015), in validating a model for PV performance based upon shading inputs, specifically identify the uncertainty of obstacle identification as a key area for future work, stating: "slight mistakes in obstacle sizing or placement may have a large impact on annual performance prediction." In this paper, we will describe a methodology that was employed to investigate the impact

of these horizon measurement uncertainties on calculations of the predicted output of a photovoltaic installation.

2. Background

2.1. Modelling of the Shaded Irradiance

Modelling the impact of shading on a solar panel typically is performed in a two-step process (Goss et al., 2014). The impact of obstructions on available irradiance is determined via geometric calculations related to the horizon, the sun position and the collector field of view. Irradiance reduction may be considered for an entire module, with approximations used to consider its spatial distribution or on a cell-by-cell basis (Goss et al., 2014; Quaschning and Hanitsch, 1995). Models exist for computing an adjusted irradiance based upon the shading at each point (Drif et al., 2008). The adjusted irradiance results can then be used as an input to an electrical model that simulates the PV module performance in terms of the electrical performance of each cell under variable irradiance (Bai et al., 2015; Bishop, 1988; Ishaque et al., 2011), aggregated by modelling connections between cells and strings. This paper deals primarily with the first part of the process: determination of the reduced irradiance.

Models of solar irradiance on a tilted collector consider the solar resource to be the sum of beam, diffuse and reflected-diffuse components (Muneer, 2004; Perez et al., 1990):

Eq 1. $$G_t = G_{bt} + G_{dt} + G_{gt}$$

Further, the diffuse irradiance may at times be considered to include isotropic, circumsolar (i.e. beam-like) and near-horizon components.

Eq 2. $$G_{dt} = G_{d,iso} + G_{d,cir} + G_{d,hor}$$

Shading affects both direct and diffuse irradiance components, but may be expected to influence the different components of the resource in different ways. The most common approach to analyze the differential shading effects is to determine separate beam and diffuse shading factors (Drif et al., 2008; Quaschning and Hanitsch, 1995) which vary between zero (shaded) and one (unshaded). The generic definition of a shade factor is the ratio between shaded and unshaded irradiance:

Eq 3. $$f = \frac{G_{sh}}{G}$$

As stated, separate shading factors may be used to describe the effect of shading on the beam and diffuse irradiance. The beam shading factor (f_b) represents the direct obstruction of the sun by an obstacle. As a result, it depends heavily on the sun position and must usually be calculated in a time dependent fashion. One method for calculation of the beam shading factor is by testing sun positions to determine whether they are located above or below a known horizon. On the other hand, the diffuse shading factor represents the reduction in the view factor between the sky and the collector caused by the horizon. That is, the hemispheric blue sky diffuse irradiance must be reduced to account for obstructions that hide portions of the sky dome. As a result, for a stationary collector, the diffuse shading factor can essentially be considered as constant with respect to time, as it is independent of the

sun position. It may be computed using the following integral, considering all diffuse irradiance to be isotropic, adapted from literature (Quaschning and Hanitsch, 1995):

Eq 4. $$f_d = \frac{\iint S(\gamma,\alpha)\cos\theta\cos\alpha\ \mathrm{d}\alpha\ \mathrm{d}\gamma}{\pi(1+\cos\beta)/2}$$

In this equation, the terms α and γ are the altitude and azimuth, respectively, for a patch of sky. The factor $S(\gamma,\alpha)$ represents the shading function, which takes a value of zero or unity, describing whether or not a patch of sky is shaded on an azimuth and altitude basis. The incidence angle, θ, is computed between the patch of sky at α and γ and the collector (oriented at a tilt of β and an azimuth of γ_c).

Multiple approaches exist for applying the shading factors and computing their influence on the irradiance. The primary differences between approaches occur in the interpretation of the beam shading factor: whether the beam shading factor is considered to be binary or allowed to take fractional values, and whether the beam shading factor is considered to apply only to the beam irradiance or to both the beam and circumsolar diffuse components.

Allowing the beam shading factor to take only binary values implies an infinitesimal (i.e. single point) collector for which the sun is either completely obstructed or not for the entire time period. The possibility of fractional values could be used to model a variety of physical phenomena: partial obstruction of the sunlight, shading for only a portion of the time step, or shading of only part of the collector. As to the second difference, some approaches only consider the beam shading factor to reduce the beam (direct) irradiance, but approaches have been proposed in which the diffuse circumsolar component is lumped with the beam irradiance, rather than the isotropic diffuse, and is affected by the beam shading factor (Drif et al., 2008). For details on the approach used in this study, see Sections 3.2.1 and 3.2.2.

2.2. Tools for Measurement of the Horizon

One category of methods for assessment of the shading requires knowledge of the local horizon in terms of azimuth and altitude of obstructions to the sky. Studies have been conducted to make use of Digital Elevation Maps, such as those generated from satellite data, to compute these local horizons over large geographic areas (Dozier and Frew, 1990). Depending on the resolution of the source data, Digital Elevation Model-based computations of shading may be limited in their ability to resolve small obstacles (e.g. trees, telephone poles) that may also impact the irradiance. As a result, local measurements of the horizon are often made to obtain more detailed horizon data.

The most reliable horizon measurements of this type would be made using surveying equipment, such as a total station, capable of measuring the azimuth and altitude of obstructions around a proposed installation with a high degree of accuracy. For many applications, this level of detailed measurement may be cost prohibitive or impractical, and as a result, a variety of tools and methods have been developed that allow measurements of a horizon to be made with a smaller and/or less expensive set of instruments. Orioli and Gangi (Orioli and Gangi, 2012) detail a method by which the sun path can be visualized on photographs taken with a known orientation. Digital image processing techniques have been documented that could allow automated processing of these types of

photographs for identification of obstacles (Laungrungthip et al., 2008). Several proprietary tools such as the Solar Pathfinder (Solar Pathfinder, 2008) or the Solmetric Suneye (Solmetric Corporation, 2011) use a variety of electronic sensors along with photographic data to obtain measurements of the horizon. Ranalli (Ranalli, 2015) discussed the use of Android smartphone and its array of onboard sensors to make a visual tracing of a horizon. Recent versions of System Advisor Model (SAM) (Blair et al., 2014) also include a tool to generate a horizon based upon a 3D model of the local site, built from simplified geometric structures. Duluk et al. (Duluk et al., 2013) compare and contrast several of the tools available and note limitations associated with their practical applications.

Detailed data about the uncertainty of these techniques is not widely available. In discussing the use of smartphone onboard sensors, Ranalli (Ranalli, 2015) made a determination of the "practical use" repeatability of smartphone horizon measurements, including both systematic and user errors. This error analysis indicated that the azimuth of a measurement could be expected to have a higher uncertainty than the altitude. Measurements of the azimuth of horizon objects (e.g. a tree) could be repeated with a standard deviation of 5° and a worst case deviation of approximately +/- 10°, while altitude measurements repeated within +/- 0.5°. This finding was similar to that of Blum et al. who attribute the azimuthal errors in smartphone sensors primarily to magnetic interference in the readings of magnetometer sensors on which digitally obtained azimuths are based (Blum et al., 2013). A second observation made by Ranalli was that uncertainty was not purely random in that obstacles could experience azimuthal shifts of approximately 10° while retaining their rough overall shape. That is to say, small objects on the horizon maintain their approximate shape, but may be moved in absolute position. For this to occur, the horizon as a whole would have to either experience a uniform azimuthal shift, or acquire cumulative errors throughout the measurement that "stretch" the horizon on a local basis. This observation suggests the possibility of modelling the impact of horizon measurement error by looking at the movement of obstacles.

2.3. Technoeconomic modelling of the PV Installation

A number of tools are available to model the performance of PV systems, accepting shading factors or horizon measurements as inputs. The tool used in this study, System Advisor Model (SAM), developed by the National Renewable Energy Lab, is a freely available technoeconomic modelling application for a variety of renewable energy technologies, including PV (Blair et al., 2014). SAM requires solar resource data (e.g. Typical Meteorological Year) and a description of the proposed PV system (including shade factors) as inputs. It produces calculations of incident irradiance and power produced, as well as a variety of financial outputs. A development kit called the SAM Simulation Core (SSC) allows SAM calculations to be performed within custom software (National Renewable Energy Lab, 2014). The methodology used by SAM for these calculations is publicly documented (Gilman, 2014). Further, SAM has been validated and compared to a variety of other common commercial PV modelling tools (Freeman et al., 2014). Modelling tools like SAM that rely on horizon measurements may be expected to be subject to the common computing problem of "garbage-in, garbage-out." That is, uncertainty in the horizon measurement will result in uncertainty in the modelled PV system performance.

The purpose of this study is to investigate the sensitivity of the output of PV modelling tools (in this case SAM), subject to the type of variations in the horizon that may be encountered as a result of low-fidelity horizon measurements. Due to the high number of input parameters in PV modeling tools, this analysis was performed empirically, by observing the effect of a simulated variable horizon on the outputs of a SAM model to infer the associated sensitivity to error.

3. Calculation Methodology

In this study, we applied existing modelling tools to estimate the performance of PV arrays subject to simulated variable horizon conditions. This allowed determination of the impact that errors in the horizon measurement would be expected to have on these calculations. The SAM software development kit was used to model performance and output of a simulated PV system. We considered the sensitivity to measurement uncertainty of both annual incident irradiance and annual AC energy produced for a hypothetical array. For all sites and shading conditions tested, annual energy was found to be strongly correlated to annual irradiance ($R^2 \geq 0.9996$). As such, only computations of the annual irradiance will be reported for clarity. The following sections detail the methodology used to generate these estimates.

3.1. Simulated Horizons

Two types of horizons were used to simulate the uncertainty of a measured horizon. First, a series of simulated obstacles was generated based upon a given central azimuth, φ_c, azimuthal width, φ_w,and peak altitude (height), φ_h. Shifts in these three parameters were used to simulate error in the measurement of the object position. The obstacles simulated for this study used a flat-top shape. While this represents a hypothetical obstacle, rather than a real expected shape on the horizon, it simplifies the shading calculations and provides general insight that will be followed up with actual horizon data. That is, in addition to the simulated obstacle, an actual horizon was measured at a sample solar installation site, and was scaled and shifted to simulate measurement error. A detailed discussion of how the object position and shape parameters were varied may be found in Section 3.3, and a sample depiction of an obstacle can be found in Figure 1.

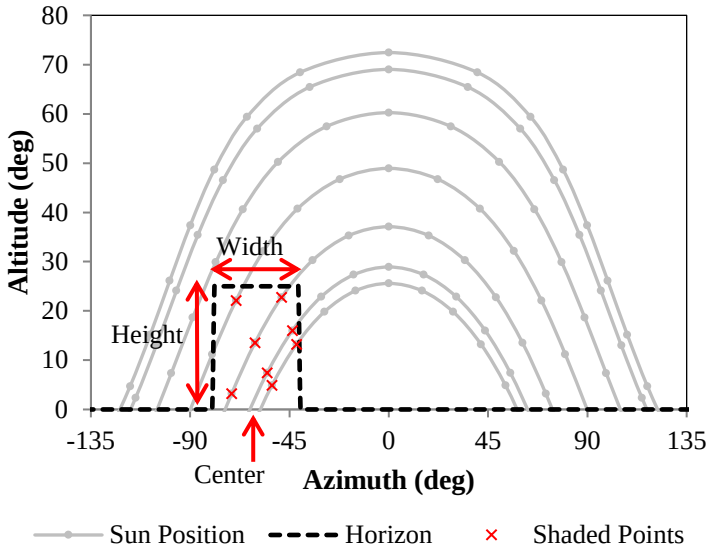

Figure 1 – Depiction of a sample horizon obstacle that results in shading, with center, width and height labelled. Adapted from Ranalli (Ranalli, 2015).

In addition to the synthetic flat top obstacle that was tested, additional simulations were conducted using a measured horizon. This horizon was measured using SolarSurvey (Ranalli, 2015), but was found to be similar to Solmetric SunEye measurements taken in the same location. SolarSurvey is a smartphone app in which users trace a horizon using the phone's camera with an augmented reality display. The Solmetric SunEye uses fisheye lens photographs to obtain a horizon. In typical use cases, SolarSurvey uses a greater number of points to represent the horizon (the SunEye uses peak altitude in 1° azimuth bins). Both techniques obtained very similar gross horizon shape, with differences occurring primarily as position shifts at the small detail level. As SolarSurvey had more information about its uncertainty available, its measured horizon was used as the reference for error estimation. Errors in the measured horizon were simulated in azimuth and altitude only. We varied azimuthal position by adding a shift to all azimuths in the measurement (wrapping at 180°), and varied height by adding a shift to the altitude of the entire horizon. A plot of the real horizon profile as measured (i.e. prior to any shifting) is shown in Figure 2.

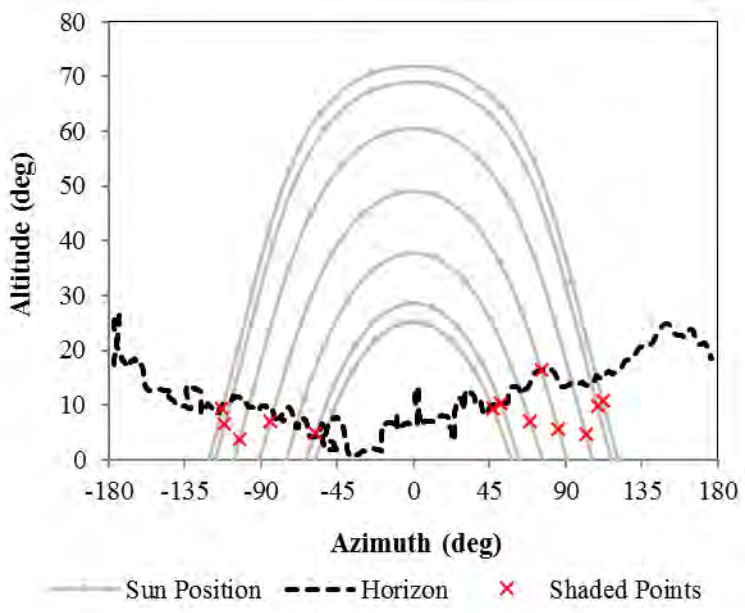

Figure 2 - Measured horizon used for testing relative to practically measured data.

3.2. Determining if a point is shaded

Horizon profiles were generated as a list of azimuth, altitude pairs representing a series of angular points on the horizon. In each horizon profile, the starting point was repeated at the end of the list in order to ensure that the horizon represented a closed polygon. To determine whether any given sky position was shaded by this horizon, a point-in-polygon algorithm was used (Chamberlain and Duquette, 2007). To test an arbitrary point, a ray was traced from straight below the observer (i.e. altitude = -90°) upward to the point of interest. Intersections between the ray and the horizon were counted, and the parity of the number of intersections reveals whether or not the tested point lies within the polygon represented by the horizon. Full details of the algorithm used may be found in a previous article describing the methodology (Ranalli, 2015).

3.2.1. Beam Shade Factors

In this study, SAM was used to determine the sun positions for each hour within a Typical Meteorological Year (TMY) file from the National Solar Radiation Database (NSRDB) (Wilcox, 2012). SAM automatically identifies hours for which the sun is entirely below 0° altitude, which are assumed to be completely shaded. For hours during part or all of which the sun has an altitude greater than 0°, SAM reports sun positions based upon hourly midpoints (e.g. data collected ending at 10:00 is represented by sun position at 9:30). The sun position reported by SAM for each hour of the year was tested against the horizon for shading. If the sun position was shaded, the beam shade factor was assigned a value of f_b = 0. Otherwise, if the position was not shaded, the beam shade factor took a value of f_b = 1.0. This model implies that any hour that experiences shading at its midpoint is assumed to be completely shaded throughout its entire duration (called Whole Hour Shading here). The beam shading factor methodology

used by SAM reduces only the beam irradiance, and does not consider the beam shade factor to reduce the circumsolar diffuse irradiance (Gilman, 2014). As stated previously, because f_b has a time dependence for each hour, this equation must be evaluated hourly and summed to yield the annual result.

Eq 6. $$G_{bt,sh}(annual) = \sum_{hourly} f_b * G_{bt}$$

In order to produce results that are most easily interpreted, the annual shaded beam irradiance was normalized by its unshaded counterpart.

Eq 7. $$G^*_{bt,sh} = \frac{G_{bt,sh}}{G_{bt}}\Big|_{annual}$$

3.2.2.Diffuse Shade Correction Factors

The diffuse shading factors were determined for a given horizon by integrating Eq. 4 numerically. A grid of patches (azimuth and altitude pairs) was generated representing the sky dome. A spacing of 1° in azimuth and 0.5° in altitude was used, with patches represented by the central angular position. The shading function, $S(\gamma, \alpha)$, was computed for each sky patch by testing whether the center azimuth and altitude of that patch was shaded, using the point-in-polygon shading algorithm discussed previously. The incidence angle, θ, was calculated for each sky patch in order to compute $\cos\theta$. Patches with incidence angles greater than 90° were also assigned a shading function value of zero, to denote patches behind the collector.

Sensitivities of the diffuse shade factor would be expected to depend upon the orientation (tilt and azimuth) of the collector. This is due to the cosine incidence angle effect, where each particular "patch" of sky has a different influence on the diffuse shading factor. Figure 3 shows that portions of the sky dome closest to the collector normal make a larger contribution to the overall diffuse irradiance seen by the collector. Consequently, obstacles that interfere with regions near the collector normal have the largest influence on the diffuse shade factor.

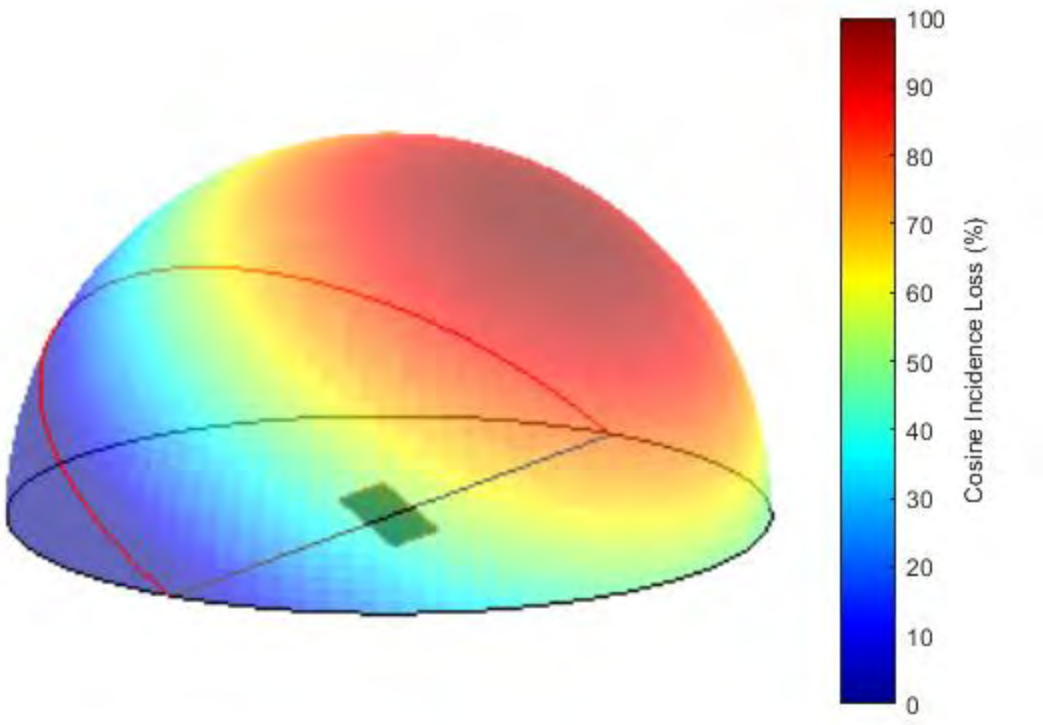

Figure 3 - Contribution of each sky patch to the isotropic diffuse irradiance seen by a collector at the sketched tilt and azimuth. The red line indicates the plane of the flat-plate collector, behind which no light collection is possible.

SAM applies the diffuse shade factor linearly to the entire diffuse irradiance term (Gilman, 2014). This method considers all diffuse components to behave isotropically from a shading perspective, and neglects any effect of the diffuse shading factor on the ground reflected irradiance. An alternative approach, such as that proposed by Drif et al. (Drif et al., 2008), might be to consider the circumsolar as part of the beam irradiance for shading purposes. Since f_d depends only on the horizon and collector geometry, its value is constant with respect to time. As such, we may write the shaded diffuse irradiance on an annual basis as follows:

Eq 8. $$G_{dt,sh}(annual) = f_d * G_{dt}(annual)$$

This implies that the sensitivity of diffuse irradiance to horizon measurement angle, $dG_{dt,sh}/d\varphi$, is linearly related to the sensitivity of the diffuse shade factor, $df_d/d\varphi$.

3.3. Determining the sensitivity of irradiance to horizon uncertainty

The annual irradiance's sensitivity to angular error in the horizon measurement can be summarized as follows, using all annual quantities.

Eq 9. $$\frac{dG_{t,sh}}{d\varphi} = \frac{dG^*_{bt,sh}}{d\varphi} G_{bt} + \frac{df_d}{d\varphi} G_{dt}$$

Since the hourly unshaded values of G_{bt} and G_{dt} are functions of the collector orientation, each of these terms may be expected to depend on the collector orientation; however, they are independent of the obstacle positions. Dependence on obstacle position is introduced through the shading factor sensitivity only. Results for $\frac{dG_{t,sh}}{d\varphi}$ will be reported normalized to the annual unshaded tilt irradiance, G_t, such that uncertainty will be reported as a percent of annual unshaded irradiance per degree.

The impact of shade factor on annual irradiance (specifically for the beam case) was found to be highly sensitive to the absolute position of the obstacle. This can be best considered by inspecting an annual plot of the sun position, as seen in Figure 4. The analemmas that are visible in this figure are an artifact of the hourly input data, typical of that available from the NSRDB. Each analemma represents the sun position at a fixed hour (e.g. 11:00 AM) throughout the entire year. A shaded hourly point can be visualized as subtracting the contribution of that shaded point from the annual irradiance.

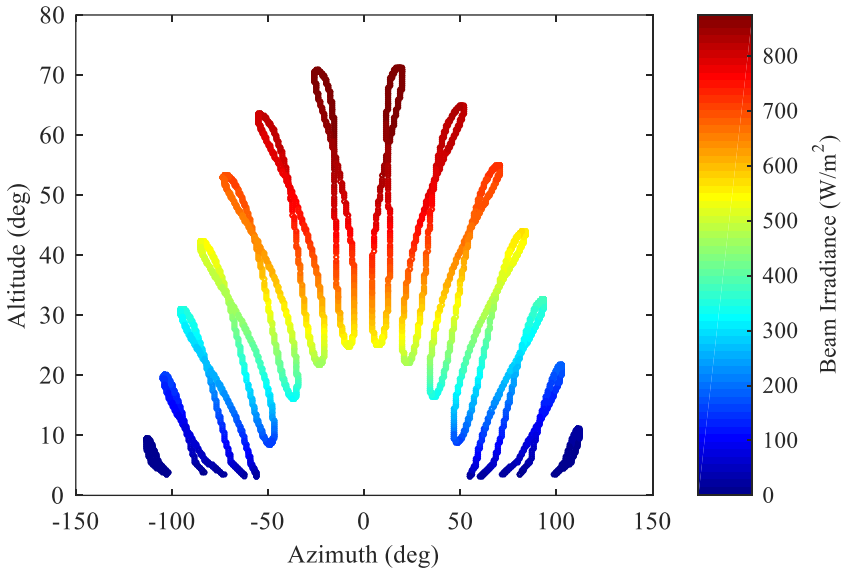

Figure 4 – All sun positions in a year, colored by beam irradiance. Colors for beam data come from Bird Clear Sky results for Wilkes-Barre, PA.

When considering the sensitivity of this process on obstacle position, we can immediately observe that obstacles positioned outside the sun path will not result in any reduction of beam irradiance. We may also infer that due to the hourly gaps between each analemma, fluctuation of the sensitivity is expected. That is to say some small obstacle movements will result in no change in the expected irradiance, as the movement occurs "between" hours. Other small obstacle movements result in very large sensitivities as obstacles suddenly shade a large number of hourly beam data points. As a result, identifying the maximum sensitivity possible for beam irradiance to object position is impossible in that it is a strong, nonlinear function of the magnitude of the object's movement. However, it was observed that these worst case uncertainties were extremely unlikely to occur across the wide range of obstacles tested. Further, for the entire range of obstacle sizes and positions computed, the probability distribution of a randomly positioned obstacle producing a given sensitivity was found to remain

approximately constant with respect to sampling resolution used in generating the obstacles. This is demonstrated in Figure 5, which shows that the CDF of sensitivity was relatively constant with varying object height shift magnitude. Similar results were observed for changes in both object center, and width.

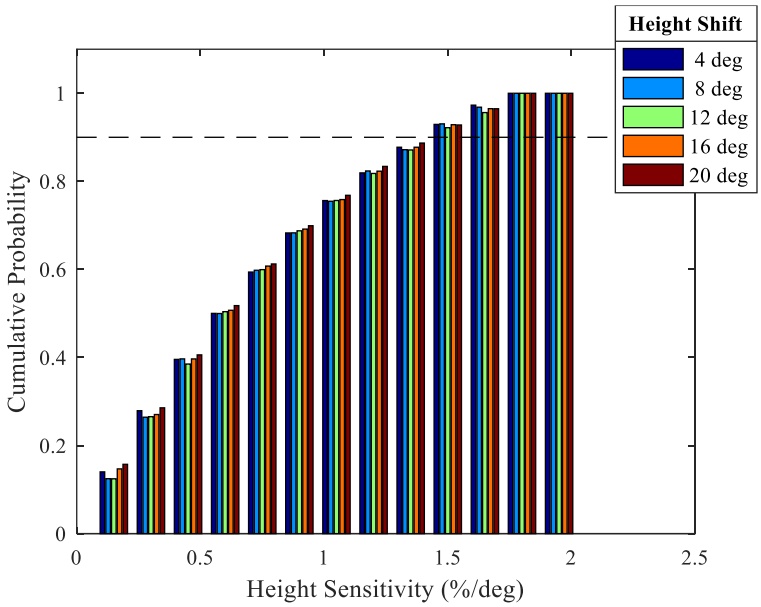

Figure 5 – CDF histogram of sensitivity of normalized beam irradiance $(G^*_{bt,sh})$ to shift in obstacle height for various obstacle shift magnitudes. Colored bars represent shifts from 4° up to 20°. The dashed line shows the P90 level. Collector tilt is 25°, and collector azimuth is 0° (south).

Because the maximum value is impossible to ascertain precisely for the reasons stated, we describe the expected sensitivity to obstacle position error using the mean sensitivity and a P90 sensitivity metric. This P90 metric identifies the level at which 90% of the possible sensitivity values encountered should be less than the indicated value. P90 values were calculated ignoring sensitivity values of exactly zero (primarily where the irradiance was not at all shaded by the obstacle). Simulations were conducted with a 10° increment in each of the obstacle parameters for both diffuse shade factor and beam factor results, as shown in Table 1. Note that though some of the obstacle sizes may not be realistically encountered in actual solar power installations (e.g. a 180° wide 90° tall obstacle essentially obstructs the entire southern sky), we compute sensitivities over a large range of obstacles to observe limiting cases. Sensitivities to each variable were computed, along with an overall sensitivity, calculated using the magnitude of the gradient vector.

Table 1 - Obstacle limits used to produce the data

Parameter	Limits	Increment
Center	-180° to +180°	10°
Width	0-270°	10°
Height	0-90°	10°

4. Results

4.1. Diffuse Shade Factor

The diffuse shading factor was computed as a function of four variables: obstacle center, width and height, along with collector tilt. Figure 6 shows contours of the diffuse shade factor with variation in each of these independent variables. Intuitively, obstacles that are large (both in height and width) produce the largest reductions in values of the diffuse shade factor. Additionally, we can observe that the largest reductions occur when the obstacle is centered relative to the collector azimuth, and that the diffuse shade factor is affected more strongly with increasing tilt. While these trends are instructive in understanding how obstacles affect the diffuse shade factor, the most important consideration when identifying the effect of horizon measurement errors is actually the sensitivity with respect to each variable (i.e. the directional derivatives on contours such as these).

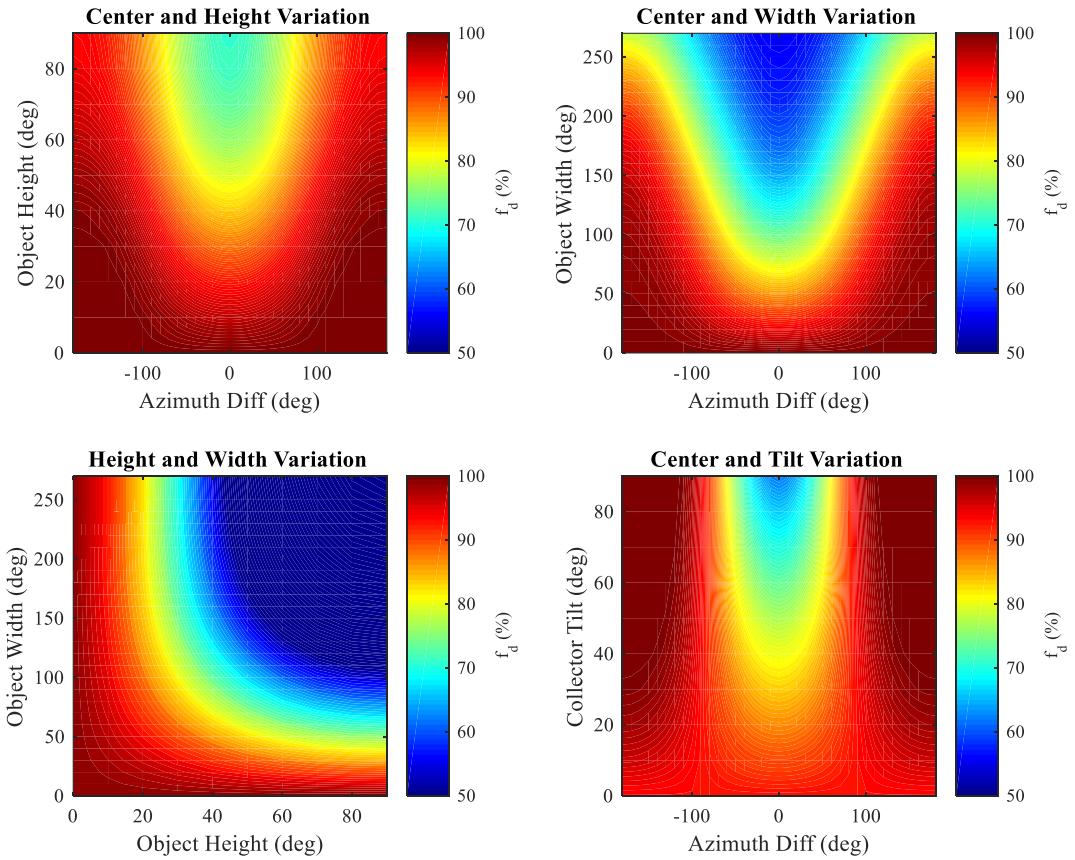

Figure 6 – Magnitude of diffuse shade factor with various independent variable variations. Values for each variable when held constant are: tilt of 30°, width of 60°, height of 40° and center difference of 0°.

Contour plots of *sensitivity* to each independent variable as a function of obstacle center and height (i.e. at a fixed width and tilt) are shown in Figure 7. Though some slight variation in the character of these plots was observed as obstacle width and collector tilt varied, they held sufficiently constant that they can be described generally here. Diffuse shade factor is most sensitive to changes in object central position for objects that are located at the edges of the collector field of view (i.e. near +/- 90°).

Generally, sensitivity to height and width reaches a peak for objects that are directly in front of the collector. However, for objects approaching 180° in width, the peaks in width sensitivity occur at the edges of the collector's field of view.

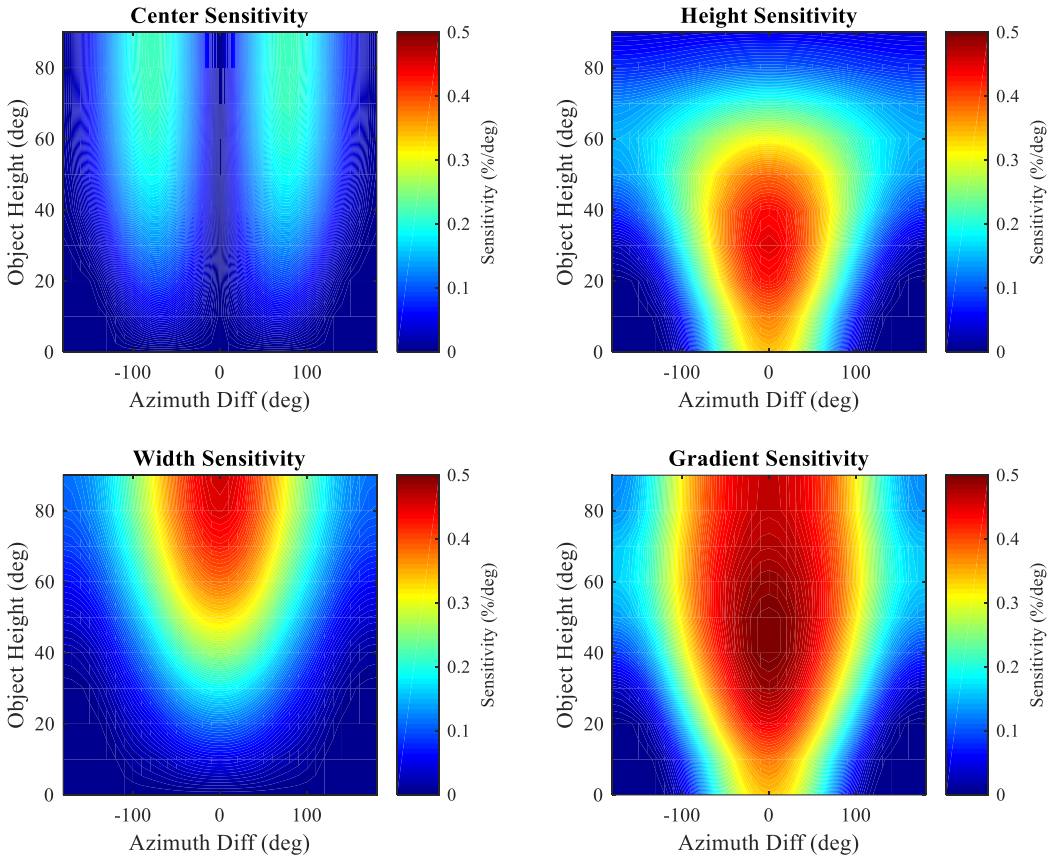

Figure 7 – Sensitivity of diffuse shade factor to changes in obstacle parameters for a collector of tilt 30° and obstacle width of 60°.

It may be more instructive to consider the variation in these sensitivities relative to each variable by looking at statistical values based upon the probability of any given sensitivity value being observed across a global set of obstacle height, width and position variations. We compute P90 values, which represent a conservative estimate of the sensitivity from all other variables. For example, when considering trends as the obstacle height varies, the P90 sensitivities trend toward the worst case sensitivities with respect to center, width and tilt simultaneously. Trends in P90 sensitivity with respect to each variable individually are shown in Figure 8. Though it is clear that the worst-case sensitivities do not obey simple relationships, a few general comments can still be made. Objects that are tall and narrow demonstrate the lowest sensitivity to each kind of obstacle position errors, as do objects that are located beyond the field of view of the collector. In the worst cases, height is more sensitive than width for obstacles centered on the collector azimuth. We can also observe that overall, the sensitivity to obstacle position errors increases with increasing collector tilt.

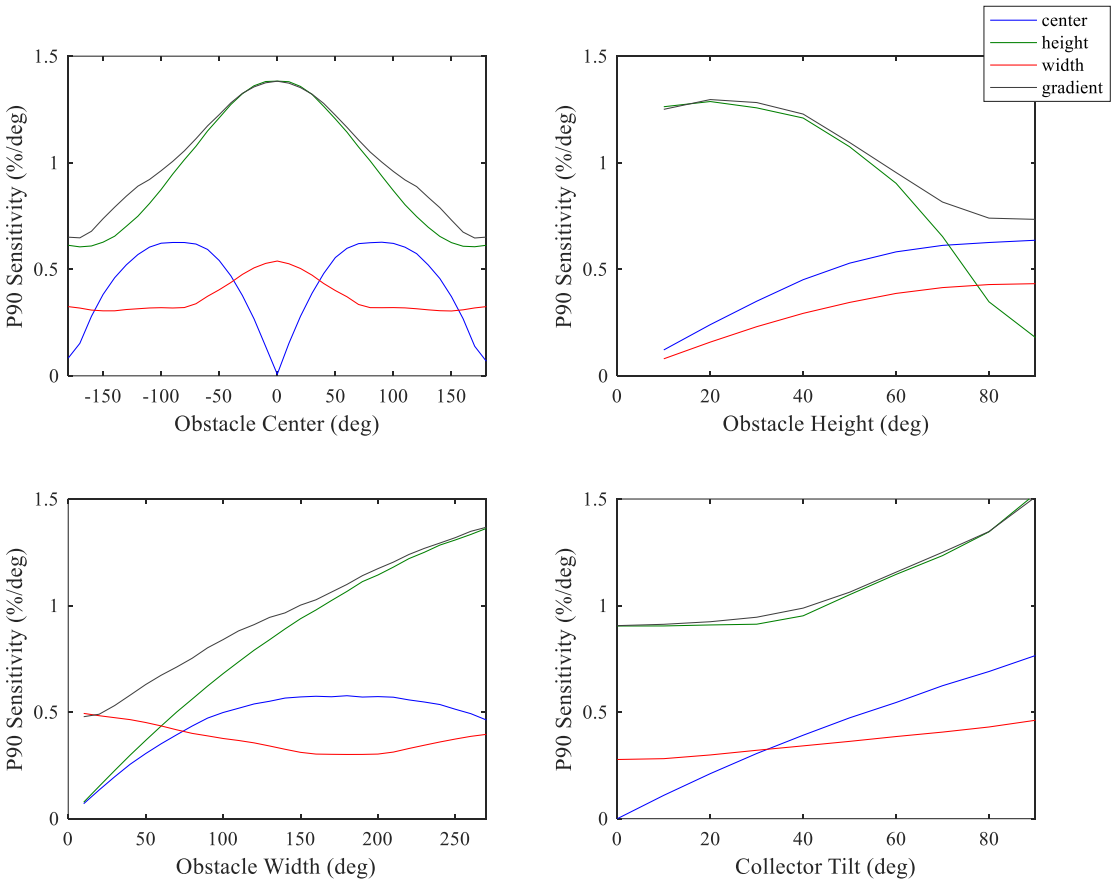

Figure 8 – P90 sensitivity of diffuse shade factor, relative to each parameter studied

Numerical values for the global P90 and mean sensitivities are given in Table 2. These sensitivities were calculated across all tested conditions. Thus they can be viewed as the P90 and mean sensitivities that could be expected given a random obstacle position, height and width. Again, in this context, P90 may be interpreted as a conservative estimate for the uncertainty with respect to each obstacle position variable.

Table 2 –Derivatives in f_d per degree error in each obstacle position parameter (any tilt, any obstacle)

	P90 Sensitivity (%/deg)	Mean Sensitivity (%/deg)
$\frac{df_d}{d\varphi_c}$	0.50%	0.15%
$\frac{df_d}{d\varphi_h}$	1.04%	0.39%
$\frac{df_d}{d\varphi_w}$	0.36%	0.16%
$\frac{df_d}{d\varphi}$	1.06%	0.52%

The sensitivity to a practical horizon was also evaluated as described previously. Results for sensitivity to both azimuth and altitude variation are given in Table 3. These values are comparable in magnitude to those observed for the single obstacle horizon, and overall represent a relatively low sensitivity to error. We still observe that measurements are more sensitive to errors in the altitude measurement, however the sensitivity to azimuthal variations is observed to decrease as compared to the top-hat horizons, while the sensitivity to altitude increases.

Table 3 –Derivatives in f_d per degree error for the measured horizon (any tilt)

	P90 Sensitivity (%/deg)	Mean Sensitivity (%/deg)
$\frac{df_d}{d\varphi_c}$	0.11%	0.04%
$\frac{df_d}{d\varphi_h}$	1.60%	0.99%

Referring to Eq 8 previously, we can apply these diffuse shade factor uncertainties to directly represent the uncertainty in diffuse irradiance. In this case, we observe that for the top-hat profile, the P90 expected sensitivity of diffuse irradiance is around 1% based upon the magnitude of the gradient (1.6% considering the real horizon results), while the mean expected sensitivity is around 0.5%. We are most interested in the combined sensitivity of these calculations to errors in an actual measurement of the horizon. This sensitivity depends on the indicated uncertainty of the measurement. While each horizon measurement device/technique might be expected to have unique uncertainty values, we can use the values reported by Ranalli (Ranalli, 2015) which describe a relatively imprecise horizon measurement device (an Android smartphone). Ranalli shows that standard deviation for this device's horizon measurement repeatability was approximately +/- 5° for azimuth and +/- 0.5° for altitude. Applying these values in a standard propagation of uncertainty procedure (Eq 10 below), considering azimuth as the applicable measurement for center and width, and altitude for height, yields an uncertainty value of approximately 3% based upon the P90 sensitivity, and 1% based upon the mean sensitivity. For the data based upon the actual measured horizon, a similar analysis produces values of 1% by P90 sensitivity and 0.5% by mean sensitivity. Given that in both cases, calculations are most sensitive to obstacle heights, techniques that have a larger uncertainty of altitude measurement would be expected to experience higher levels of overall uncertainty.

Eq 10. $$\sigma_{diffuse} = \sqrt{\left(\frac{df_d}{d\varphi_h}\right)^2 {\sigma_{alt}}^2 + \left[\left(\frac{df_d}{d\varphi_c}\right)^2 + \left(\frac{df_d}{d\varphi_w}\right)^2\right] {\sigma_{az}}^2}$$

4.2. Beam Shade Effects

A similar procedure was carried out to map the sensitivity of the beam irradiance to errors in obstacle position. One additional challenge facing the beam irradiance was that beam irradiance depends strongly on the hourly beam irradiance distribution, which is typically calculated from the appropriate

input meteorological data file. To generalize the results here, we compared results from seven US cities (listed in Table 6), along with Bird Clear Sky model meteorological inputs for one of the cities. Results from each city were closely comparable, and as such, graphical data will be shown for Wilkes-Barre, Pennsylvania as a representative case.

Figure 9 shows contours of the beam irradiance with respect to the size and position of shading obstacles tested. Annual beam irradiance is itself a strong function of collector tilt and azimuth, and as a result of this confounding factor, collector orientation was not considered as a variable for beam irradiance sensitivity. A fixed "typical" collector oriented at 25° tilt and 0° azimuth was used for all beam sensitivity calculations. As was the trend with the diffuse shade factor, larger obstacles (in both height and width) produce a greater reduction in the beam irradiance. For short obstacles (i.e those that do not at all affect the noontime sun even during winter), the beam irradiance is most affected by obstacles centered near +/- 90°, however, these reductions are relatively small. Taller obstacles that do begin to obstruct the noontime sun produce the largest reductions in beam irradiance when centered near geographic south.

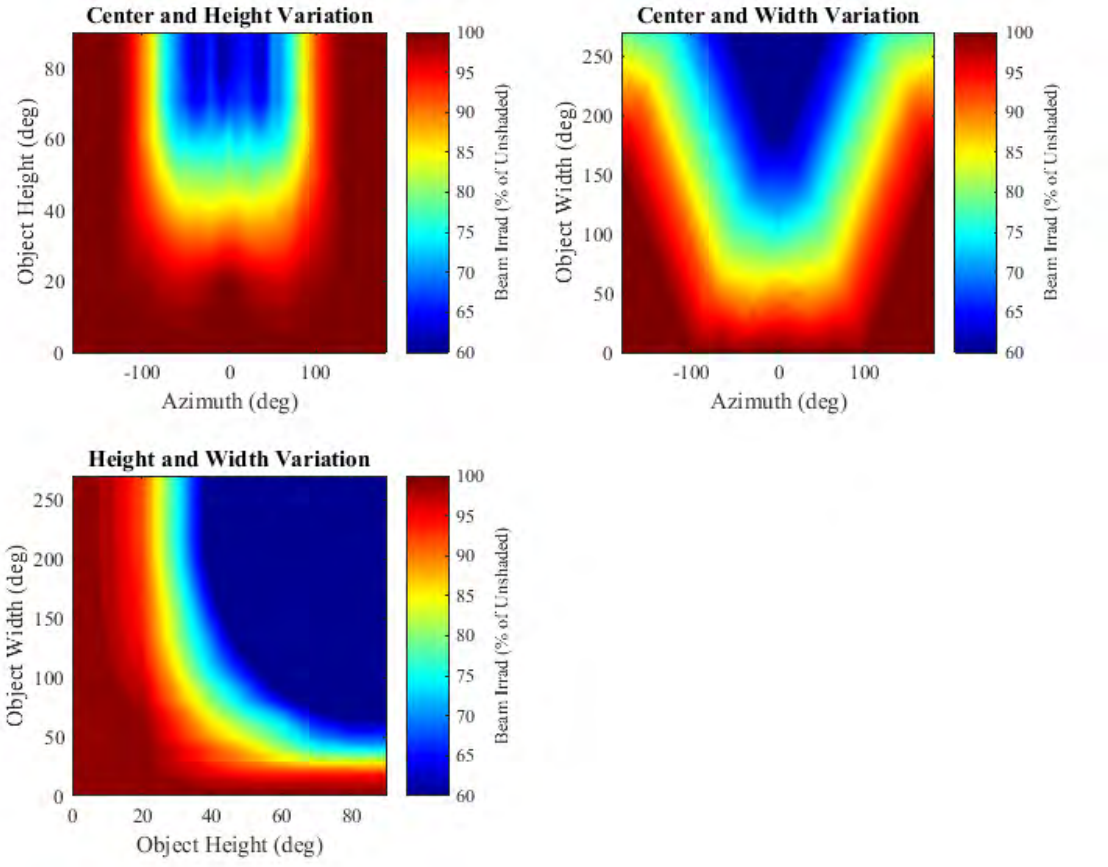

Figure 9 - Annual beam irradiance subject to variation in each independent variable at a fixed tilt of 25°, for Wilkes-Barre, PA TMY3 data. Values for each variable when held constant are: width of 60°, height of 40° and center of 0°.

As before, we are most interested in the sensitivities of annual beam irradiance to obstacle position, which can be investigated through the directional derivatives as measured from the full set of obstacle position variation contours. Figure 10 depicts contours of the sensitivity of annual beam irradiance to each obstacle position variable, as well as the magnitude of the gradient vector. However, caution should be used when interpreting these contours, due to the nonlinear relationship between the object shift interval and the maximum inferred sensitivity discussed in Section 3.3. The fringe patterns (most notable in the bottom left and bottom right portions of Figure 10) result from essentially interference between the roughly 15° hourly sun position (see Figure 4) and the 10° obstacle parameter increment. Due to the nature of this interference, reducing the obstacle shift increment results in fringes that exhibit greater spatial variability and greater intensity. A few general trends from this figure may be instructive. Measurements are most sensitive to object central position for obstacles that are located near sunrise and sunset, i.e. in the vicinity of +/-90°. The greatest sensitivity to height is observed for obstacles around 40° tall. Sensitivity to obstacle width increases for taller obstacles.

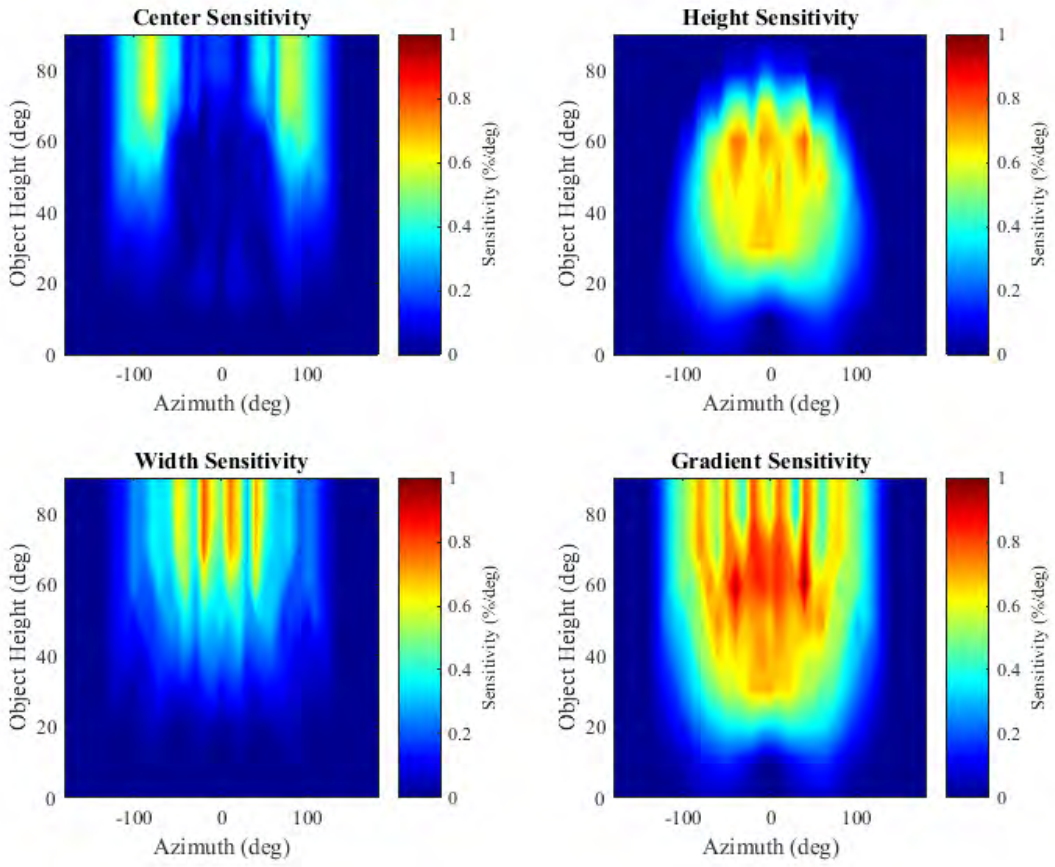

Figure 10 - Sensitivity of annual beam irradiance to each object position variable as a percent, for a collector tilted at 25°, and an obstacle width of 60°. TMY3 data used for Wilkes-Barre, PA.

We can also consider trends in the P90 sensitivity as a percent of the beam irradiance to each of the three obstacle position parameters. These are shown graphically in Figure 11. The overall trends shown

in these graphs are similar to those described for diffuse shade factor, albeit with slightly larger magnitudes. Narrow objects have the lowest sensitivity to any obstacle measurement uncertainty. In the case of beam irradiance, objects that are either very tall or very short also demonstrate low sensitivities. In terms of center position, errors are reduced for objects located beyond the field of view of the collector, and outside the path of the sun. As with diffuse irradiance, we see that irradiance calculations are more sensitive to obstacle height than width or central position for most conditions. A summary of the P90 and mean sensitivity metrics for Wilkes-Barre are provided numerically in Table 4.

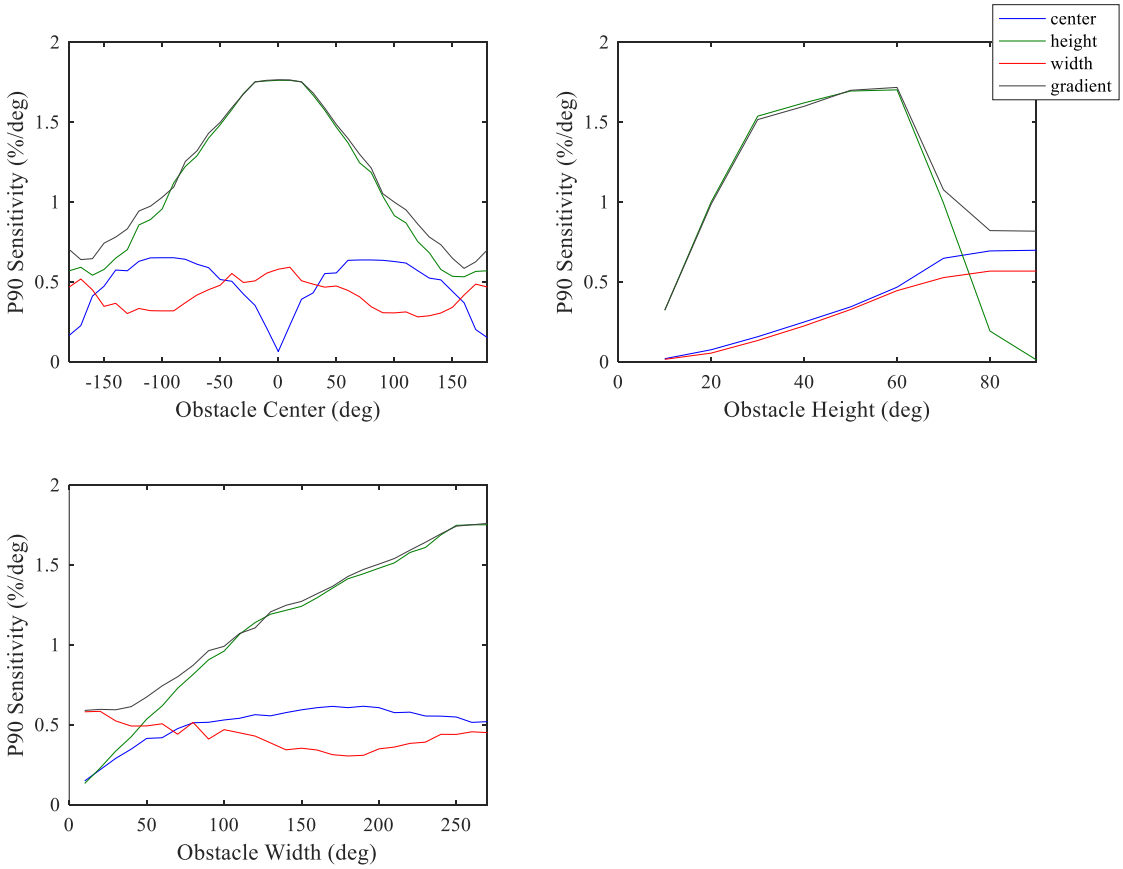

Figure 11 - Plots of the P90 sensitivity for each variable for Wilkes-Barre, PA. Collector tilt is 25°.

Table 4 –Sensitivity of $\frac{dG^*_{bt,sh}}{d\varphi}$ with respect to each obstacle position parameter

	P90 Sensitivity (%/deg)	Mean Sensitivity (%/deg)
$\frac{d\boldsymbol{G}^*_{\boldsymbol{bt,sh}}}{d\varphi_c}$	0.54%	0.17%
$\frac{d\boldsymbol{G}^*_{\boldsymbol{bt,sh}}}{d\varphi_h}$	1.24%	0.37%
$\frac{d\boldsymbol{G}^*_{\boldsymbol{bt,sh}}}{d\varphi_w}$	0.43%	0.14%

$\frac{d\boldsymbol{G}^*_{\boldsymbol{bt,sh}}}{d\varphi}$	1.25%	0.52%

Sensitivities to errors in the actual horizon measurement are given in Table 5. Trends match those observed when comparing the top-hat and real horizon sensitivities for the diffuse shade factor. As before, we observe that the sensitivities to azimuth for the practical horizon are lower than those seen for the simulation, while a greater sensitivity to altitude is observed. The overall magnitudes of these sensitivities are still relatively low.

Table 5 –Sensitivity of $\frac{d\boldsymbol{G}^*_{\boldsymbol{bt,sh}}}{d\boldsymbol{\varphi}}$ to the measured horizon profile uncertainty

	P90 Sensitivity (%/deg)	Mean Sensitivity (%/deg)
$\frac{d\boldsymbol{G}^*_{\boldsymbol{bt,sh}}}{d\varphi_c}$	0.36%	0.13%
$\frac{d\boldsymbol{G}^*_{\boldsymbol{bt,sh}}}{d\varphi_h}$	2.09%	1.08%

Using the same propagation of uncertainty approach applied for the diffuse shade factor (5° standard deviation in azimuth and 0.5° standard deviation in altitude), we can compute an uncertainty for the beam irradiance of 3.5% for the P90 and 1.1% for the mean for Wilkes-Barre based upon the top-hat horizon profile. For the actual measured horizon, the beam sensitivities are 2.1% for P90 and 0.9% for the mean. As before, horizon measurement approaches with a greater obstacle height uncertainty would be expected to have a greater overall uncertainty, due to the greater sensitivity to measured altitude.

4.3. Total Horizon Measurement Uncertainty

Given the annual unshaded beam and diffuse irradiance values for Wilkes-Barre, application of these sensitivities to Equation 10 gives a combined annual total irradiance uncertainty of 3.3% for the P90 sensitivities and 1.1% for the means using the top-hat profile results. They change to 2.2% for the P90 and 1.2% for the mean sensitivities when considering results from the actual horizon. As the top-hat results are more conservative, we will consider those in subsequent discussion. Table 6 shows the total uncertainty estimates based upon P90 and the mean sensitivity for all other cities tested. No strong effect of location within the continental US was observed for these sensitivities. To provide a summary interpretive statement for these calculations, for a device with a 5° azimuth uncertainty and a 0.5° altitude uncertainty, we can estimate a 90% probability of the actual annual shaded irradiance falling within 3.3% of the annual shaded irradiance predicted using the measured horizon. This is also true for the modeled array annual AC production subject to shading.

Table 6 - Comparison of annual irradiance sensitivity for all cities. Data is based upon TMY3 for location unless otherwise noted. All sensitivities are based upon the top-hat profile analysis.

	P90 Sensitivity	Mean Sensitivity
Phoenix, AZ	3.17%	1.02%
San Francisco, CA	3.21%	1.03%
Miami, FL	3.08%	0.97%

Orlando, FL	3.10%	0.99%
Chicago, IL	3.29%	1.07%
Wilkes-Barre, PA	3.27%	1.05%
Wilkes-Barre, PA (Bird Clear Sky)	3.44%	1.12%
Dallas, TX	3.13%	1.01%

Note that these sensitivities only refer to that associated with measurement of the horizon for a single point collector. In computing the overall uncertainty in the performance of a solar energy system, additional factors need to be taken into account. Uncertainty in pyranometer irradiance measurement is estimated between 4%-8% (Stoffel, 2013) depending on the type of device. When considering a variety of uncertainty sources, Thevenard and Pelland (Thevenard and Pelland, 2013) report that the combined uncertainty from all sources in the entire modelling process is around 8.7% for the first year of operation. The 3.3% shading uncertainty reported in this study is similar to the values Thevenard and Pelland use for uncertainties associated with other components of a PV performance model (e.g. insolation, climatological variation, tilted irradiance estimation, module ratings).

These estimates must also be interpreted in the context of the analysis and the tool used to conduct it. For the beam shade factor results, collector orientation was not considered as a variable, due to the difficulty in separating the effects of beam incidence angle and shading. This remains a potential area for future investigation. Additionally, SAM's use of hourly data, while common in simple solar modeling activities, results in the fringing effect described in Section 4.2. A smaller timestep, or utilizing a beam shade factor computation technique that identified fractional part-hours during which shading occurred, might serve to mitigate the fringe effect and reduce the dependence on obstacle position step size. Additionally, SAM's use of a simplified approach for diffuse irradiance (i.e. all diffuse irradiance is treated as isotropic) would be expected to change these results somewhat if a more sophisticated approach was used. In particular, if the circumsolar irradiance were considered to be part of the beam irradiance for shading purposes (Drif et al., 2008), we would expect the possibility of a greater sensitivity to the beam shading factor. However, we would expect these effects to respond in a relatively straightforward fashion relative to the amount of irradiance that is affected.

5. Conclusions

Many solar installations are subject to some degree of shading as a result of nearby terrain, structures or vegetation. Approaches exist to model reductions in solar performance due to this shading. These approaches rely on a measurement or model of the local horizon from the point of view of the solar energy collection system. In this study, we have conducted simulations of the sensitivity of shaded solar performance models to uncertainties in the horizon measurement. These simulations were based upon a flat-top obstacle with varying height, width and center position, and determined the impact of this obstacle on modeled array performance. Shifts in azimuth and altitude of an actual horizon profile were also considered.

In general, we find that diffuse and beam irradiance have similar sensitivity to errors in the horizon measurement. In both cases, and for both flat-top and actual horizons, a higher sensitivity was observed

to errors in object altitude (about 2% per degree error), than to errors in object center or width (about 0.5% per degree error), which would both be associated with the measurement azimuth. These estimates represent a conservative prediction, in that they use a 90% confidence interval relative to a random obstacle. Further, these estimates are likely to favor the lower end of the scale in practical cases, due to the fact that estimates include shading by obstacles of extreme sizes that may be unlikely in practical solar installations. Using uncertainty of a sample measurement technique from literature (+/-5° azimuth, +/-0.5° altitude), we arrive at an estimate that shaded annual performance will fall within 3.3% of predicted values (2.2% for the actual horizon). Thus, overall, we may conclude that for a single-point collector, modeled array performance is relatively insensitive to errors in the measurement of an obstacle on the horizon. Further work may be warranted to extend this approach to consider the behavior of spatially distributed shadowing that may be indicative of a finite size array.

6. References

Bai, J., Cao, Y., Hao, Y., Zhang, Z., Liu, S., Cao, F., 2015. Characteristic output of PV systems under partial shading or mismatch conditions. Sol. Energy 112, 41–54. doi:10.1016/j.solener.2014.09.048

Bishop, J.W., 1988. Computer simulation of the effects of electrical mismatches in photovoltaic cell interconnection circuits. Sol. Cells 25, 73–89. doi:10.1016/0379-6787(88)90059-2

Blair, N., Dobos, A.P., Freeman, J., Neises, T., Wagner, M., Ferguson, T., Gilman, P., Janzou, S., 2014. System Advisor Model, SAM 2014.1.14: General Description. National Renewable Energy Laboratory.

Blum, J.R., Greencorn, D.G., Cooperstock, J.R., 2013. Smartphone Sensor Reliability for Augmented Reality Applications, in: Zheng, K., Li, M., Jiang, H. (Eds.), Mobile and Ubiquitous Systems: Computing, Networking, and Services, Lecture Notes of the Institute for Computer Sciences, Social Informatics and Telecommunications Engineering. Springer Berlin Heidelberg, pp. 127–138.

Chamberlain, R.G., Duquette, W.H., 2007. Some algorithms for polygons on a sphere. JPL Publ., 07-03. doi:http://hdl.handle.net/2014/40409

Dozier, J., Frew, J., 1990. Rapid calculation of terrain parameters for radiation modeling from digital elevation data. IEEE Trans. Geosci. Remote Sens. 28, 963–969. doi:10.1109/36.58986

Drif, M., Pérez, P.J., Aguilera, J., Aguilar, J.D., 2008. A new estimation method of irradiance on a partially shaded PV generator in grid-connected photovoltaic systems. Renew. Energy 33, 2048–2056. doi:10.1016/j.renene.2007.12.010

Duluk, S., Nelson, H., Kwok, A., 2013. Comparison of Solar Evaluation Tools: From Learning to Practice, in: Proceedings of the 42nd ASES Annual Conference. Presented at the Solar 2013, American Solar Energy Society, Baltimore, MD.

Freeman, J., Whitmore, J., Blair, N., Dobos, A.P., 2014. Validation of Multiple Tools for Flat Plate Photovoltaic Modeling Against Measured Data (No. NREL/TP-6A20-61497). National Renewable Energy Laboratory.

Galli, M., Hoberg, P., 2009. Solar Site Evaluation Tools & Techniques to Quantify & Optimize Production. Sol. Pro.

Gilman, P., 2014. SAM Photovoltaic Model Technical Reference [WWW Document]. URL https://sam.nrel.gov/reference (accessed 10.14.14).

Goss, B., Cole, I., Betts, T., Gottschalg, R., 2014. Irradiance modelling for individual cells of shaded solar photovoltaic arrays. Sol. Energy 110, 410–419. doi:10.1016/j.solener.2014.09.037

Hanson, A.J., Deline, C.A., MacAlpine, S.M., Stauth, J.T., Sullivan, C.R., 2014. Partial-Shading Assessment of Photovoltaic Installations via Module-Level Monitoring. IEEE J. Photovolt. 4, 1618–1624. doi:10.1109/JPHOTOV.2014.2351623

International Energy Agency, 2015. PVPS report - A Snapshot of Global PV - 1992-2014 (No. IEA PVPS T1-2 6 :2015). IEA Photovoltaic Power Systems Programme.

Ishaque, K., Salam, Z., Syafaruddin, 2011. A comprehensive MATLAB Simulink PV system simulator with partial shading capability based on two-diode model. Sol. Energy 85, 2217–2227. doi:10.1016/j.solener.2011.06.008

Laungrungthip, N., McKinnon, A.E., Churcher, C.D., Unsworth, K., 2008. Edge-based detection of sky regions in images for solar exposure prediction, in: Image and Vision Computing New Zealand, 2008. IVCNZ 2008. 23rd International Conference. Presented at the Image and Vision Computing New Zealand, 2008. IVCNZ 2008. 23rd International Conference, pp. 1–6. doi:10.1109/IVCNZ.2008.4762101

MacAlpine, S., Deline, C., 2015. Simplified Method for Modeling the Impact of Arbitrary Partial Shading Conditions on PV Array Performance, in: 42nd IEEE Photovoltaic Specialists Conference. Presented at the 42nd IEEE Photovoltaic Specialists Conference, New Orleans, LA.

Muneer, T., 2004. Solar Radiation and Daylight Models, 2 edition. ed. Routledge, Oxford ; Burlington, MA.

National Renewable Energy Lab, 2014. SAM Simulation Core SDK | System Advisor Model (SAM) [WWW Document]. URL https://sam.nrel.gov/content/sam-simulation-core-sdk (accessed 12.23.14).

Orioli, A., Gangi, A.D., 2012. An improved photographic method to estimate the shading effect of obstructions. Sol. Energy 86, 3470–3488. doi:10.1016/j.solener.2012.07.027

Perez, R., Ineichen, P., Seals, R., Michalsky, J., Stewart, R., 1990. Modeling daylight availability and irradiance components from direct and global irradiance. Sol. Energy 44, 271–289. doi:10.1016/0038-092X(90)90055-H

Quaschning, V., Hanitsch, R., 1995. Shade Calculations in Photovoltaic Systems. Presented at the ISES Solar World Conference, Zimbabwe.

Ranalli, J.A., 2015. Solar Survey: Development and validation of a smartphone-based solar site assessment tool. Sol. Energy 122, 1199–1213. doi:10.1016/j.solener.2015.10.039

Solar Pathfinder, 2008. Instruction Manual for the Solar Pathfinder [WWW Document]. URL http://www.solarpathfinder.com/pdf/pathfinder-manual.pdf (accessed 2.17.15).

Solmetric Corporation, 2011. Solmetric SunEye 210 Series Users Guide [WWW Document]. URL http://resources.solmetric.com/get/Solmetric%20SunEye%20200%20Series%20Users%20Guide_en.pdf (accessed 2.17.15).

Stoffel, T., 2013. A Review of Measured/Modeled Solar Resource Uncertainty, in: 2013 Sandia PV Performance Modeling Workshop. Presented at the 2013 Sandia PV Performance Modeling Workshop, Santa Clara, CA.

Thevenard, D., Pelland, S., 2013. Estimating the uncertainty in long-term photovoltaic yield predictions. Sol. Energy 91, 432–445. doi:10.1016/j.solener.2011.05.006

United Nations, 2015. Adoption of the Paris Agreement. Framework Convention on Climate Change, Paris, France.

Vignola, F., Grover, C., Lemon, N., McMahan, A., 2012. Building a bankable solar radiation dataset. Sol. Energy, Progress in Solar Energy 3 86, 2218–2229. doi:10.1016/j.solener.2012.05.013

Wilcox, S., 2012. National Solar Radiation Database 1991-2010 Update: User's Manual (No. NREL/TP-5500-54824). National Renewable Energy Laboratory.